

# Atomic scale effects of alloying, partitioning, solute drag and austempering on the mechanical properties of high-carbon bainitic–austenitic TRIP steels

Jae-Bok Seol<sup>a</sup>, Dierk Raabe<sup>a,\*</sup>, Puck-Pa Choi<sup>a</sup>, Yung-Rok Im<sup>b</sup>, Chan-Gyung Park<sup>c,\*</sup>

<sup>a</sup> Max-Planck-Institut für Eisenforschung, Max-Planck-Str. 1, 40237 Düsseldorf, Germany

<sup>b</sup> Technical Research Laboratories, POSCO, 790-785 Pohang, Republic of Korea

<sup>c</sup> Department of Materials Science and Engineering, Pohang University of Science and Technology (POSTECH), 790-784 Pohang, Republic of Korea

Received 10 February 2012; received in revised form 18 July 2012; accepted 30 July 2012

Available online 23 August 2012

## Abstract

Understanding alloying and thermal processing at an atomic scale is essential for the optimal design of high-carbon (0.71 wt.%) bainitic–austenitic transformation-induced plasticity (TRIP) steels. We investigate the influence of the austempering temperature, chemical composition (especially the Si:Al ratio) and partitioning on the nanostructure and mechanical behavior of these steels by atom probe tomography. The effects of the austempering temperature and of Si and Al on the compositional gradients across the phase boundaries between retained austenite and bainitic ferrite are studied. We observe that controlling these parameters (i.e. Si, Al content and austempering temperature) can be used to tune the stability of the retained austenite and hence the mechanical behavior of these steels. We also study the atomic scale redistribution of Mn and Si at the bainitic ferrite/austenite interface. The observations suggest that either para-equilibrium or local equilibrium-negligible partitioning conditions prevail depending on the Si:Al ratio during bainite transformation. © 2012 Acta Materialia Inc. Published by Elsevier Ltd. All rights reserved.

**Keywords:** High-carbon steels; TRIP effect; Bainite; Austempering; Retained austenite

## 1. Introduction

The transformation-induced plasticity (TRIP) effect is a pathway for obtaining high-strength and tough steels with excellent formability. Conventional TRIP steels containing about 0.15 wt.% C, 1.5 wt.% Mn and 1.5 wt.% Si exploit the transformation of metastable retained austenite into martensitic or bainitic constituents to control the mechanical properties [1–4]. Conventionally heat-treated TRIP steels, processed by a two-step process, namely intercritical annealing (IA) and isothermal bainitic transformation (IBT) annealing (the latter also referred to as austempering), have a complex microstructure consisting of a soft,

ductile intercritical ferrite matrix with retained austenite ( $\gamma_R$ ), bainite, martensite and fine carbides [5,6]. The product of ultimate tensile strength (UTS) and total elongation (TE) of these alloys can be further improved by controlling thermal processing and composition, as both factors determine the stability of the metastable  $\gamma_R$ . It has been proposed that a high stability and sufficient fraction of  $\gamma_R$  are crucial for achieving a high tensile strength in conjunction with an acceptable ductility [7]. Carbides are considered detrimental in these steels (either transition carbides or cementite) as they can initiate cleavage fracture and void formation. Moreover, carbides act as sinks for C, thus reducing partitioning of C into austenite. To avoid these effects, the addition of Si to TRIP-aided steels is important [4,7]. Si has very low solubility in cementite ( $\text{Fe}_3\text{C}$ ) and hence kinetically retards precipitation during the bainitic transformation owing to its low mobility compared to that of carbon. Consequently, Si-containing TRIP steels show

\* Corresponding authors. Tel.: +49 211 6792 340 (D. Raabe), +82 54 279 2139 (C.-G. Park).

E-mail addresses: [d.raabe@mpie.de](mailto:d.raabe@mpie.de) (D. Raabe), [cgpark@postech.ac.kr](mailto:cgpark@postech.ac.kr) (C.-G. Park).

an increase in austenite stability via C partitioning which results in improved toughness and UTS [4,7]. However, Si also deteriorates the galvanizability of low-C TRIP steels owing to the formation of a very stable  $\text{Mn}_2\text{SiO}_4$  oxide film adherent to the steel substrate [8]. As a result, the steels have poor coatability [9]. To overcome this problem, the addition of Al instead of Si was suggested [9–11]. Al slows down the formation kinetics of cementite and reduces its thermodynamic stability. Hence, substituting Si by Al leads to steels with better coating behavior without sacrificing mechanical properties [10–12]. Furthermore, Al influences the activity and solubility of C in ferrite which leads to the acceleration of bainite transformation [13,14].

In order to achieve high strength and toughness, nanostructured bainitic steels, which contain a high concentration of C (0.79 wt.%), but do not form carbides, have been designed [15–17]. These steels consist of nanoscale bainitic ferrite ( $\alpha_{\text{B}}$ ) plates and metastable C-enriched  $\gamma_{\text{R}}$ . They have a strength of 2.5 GPa and a fracture toughness of 30–40  $\text{MPa m}^{1/2}$ . Following this concept, recent efforts addressed modifications of composition and processing with the aim of reducing the C content and the heat-treatment times [18,19]. Bainitic steels containing a low C content of 0.20 wt.% have great potential for lightweight sheet forming and automotive crash applications [18]. To elucidate the redistribution behavior of solute C and the formation of nanosized cementite, atom probe tomography (APT) was applied [17,19]. It was pointed out that nanoscale carbide precipitation can take place despite a high Al (1.01 wt.%) and Si (1.50 wt.%) concentration. Irrespective of the observation of nanoscaled carbides in these materials, an atomistic understanding of the alloying effects such as the Si:Al ratio, of partitioning and of the thermal treatment on the bainitic transformation in high-carbon bainitic–austenitic TRIP steels is still lacking.

APT is well suited for studying the phase transformation as it provides information on the topology and chemistry in the vicinity of  $\alpha_{\text{B}}/\gamma_{\text{R}}$  interfaces and on the partitioning behavior of elements at near-atomic resolution [17,19–26]. Previous APT studies on TRIP steels suggest that there is no redistribution of substitutional elements, such as Cr, Mn, Al and Si, at the  $\alpha_{\text{B}}/\gamma_{\text{R}}$  interface during bainitic transformation [15–19,25–27]. This observation suggested a displacive mechanism of incomplete bainitic transformation occurring under para-equilibrium (PE) [28,29] or no partition equilibrium conditions [30]. In general, PE represents a constrained equilibrium, in which C is in local equilibrium and substitutional alloying elements are considered unaffected at the phase boundaries between proeutectoid ferrite ( $\alpha$ ) and prior austenite ( $\gamma$ ) or at the  $\alpha_{\text{B}}/\gamma_{\text{R}}$  interfaces. On the other hand, alternative models have predicted the redistribution of substitutional elements during proeutectoid ferrite transformation under local-equilibrium, negligible-partitioning (LENP) conditions [31–36]. Previous publications on quaternary Fe–C–Mn–Si alloys [37,38] have studied the transition from the PE to the LENP regime and the formation of Mn spikes during the growth of

proeutectoid ferrite. This phenomenon was interpreted in terms of a reconstructive mechanism using a stationary-interface approximation and also analyzed by scanning transmission electron microscopy (STEM). Recently, a rough estimate employing area density values of a Mn concentration spike at a  $\alpha/\gamma$  interface in a Fe–Mn–C steel was made via STEM analysis [38]. Moreover, theoretical DIC-TRA calculations and APT analyses have been carried out to better elucidate which type of local equilibrium boundary condition is prevalent at the  $\alpha/\gamma$  interface in a low carbon Fe–Mn–C alloy [39]. However, no atomic-scale understanding has been achieved so far regarding compositional spikes and/or partitioning behavior of alloying elements (especially C, Si and Mn) across the  $\alpha_{\text{B}}/\gamma_{\text{R}}$  interface in high-carbon TRIP steels [13,39–41]. Therefore, a specific challenge for advanced APT analysis lies in determining the type of equilibrium conditions prevailing at the  $\alpha_{\text{B}}/\gamma_{\text{R}}$  interface and identifying the occurrence of possible solute drag effects during bainite formation.

More specifically, it is the aim of this study to elucidate the relationship between the mechanical properties and the nanostructure of steels containing 0.71 wt.% C as a function of the Si:Al ratio, austempering temperature and partitioning effects from an atomic perspective. The steels studied in this work have a bainitic–austenitic microstructure, and are referred to as super-bainitic TRIP (SB-TRIP) steels. We subject these materials to an experimental multiscale analysis from the micrometer down to the atomic regime, paying particular attention to the stability of the  $\gamma_{\text{R}}$  phase and on the redistribution of substitutional elements in the vicinity of  $\alpha_{\text{B}}/\gamma_{\text{R}}$  interfaces during the bainite transformation. We expect that an insight into the atomic nature of the occurring phase transformations and partitioning effects involved gives us a better understanding of the relevant nanostructure–property relationships in these materials.

## 2. Experimental

Three alloys with different composition were synthesized and processed. They have the same C and Mn content but different concentrations of Si and Al (Table 1). The level of impurities, such as P and S, was below  $\sim 0.05$  wt.% for all specimens. The amount of Si + Al is about 2.0 wt.% in all alloys. The Si:Al ratios are 3:1, 1:1 and 1:3. The corresponding samples are referred to as 31SB-TRIP, 11SB-TRIP and 13SB-TRIP, respectively. All as-rolled plates were rendered austenitic at 900 °C above the  $\text{Ae}_3$  temperature for 20 min, followed by isothermal holding (austem-

Table 1  
Chemical composition (wt.%) of the SB-TRIP steels designed in this study.

Steels	C	Mn	Si	Al	Si:Al	Si + Al
31SB-TRIP	0.71	1.50	1.50	0.50	3:1	2.00
11SB-TRIP	0.71	1.52	1.00	1.04	1:1	2.04
13SB-TRIP	0.70	1.52	0.52	1.46	1:3	1.98

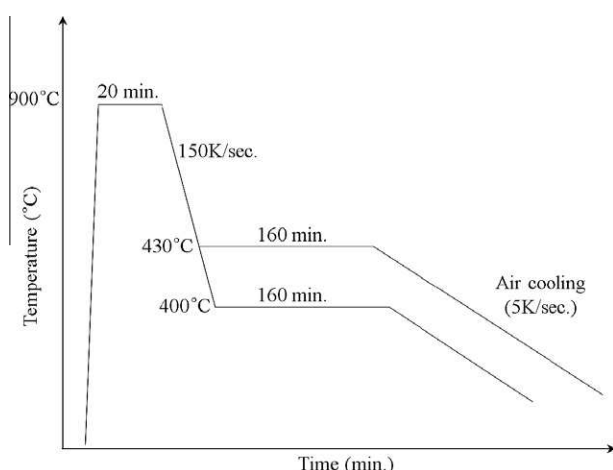


Fig. 1. Schematic illustration for the heat treatment of the studied samples.

pering) at 400 and 430 °C for 160 min in a salt bath furnace before quenching in water (Fig. 1). The cooling rate to the austempering temperature was  $\sim 150 \text{ K s}^{-1}$ , i.e. sufficient to suppress pearlite. The bainitic transformation start temperature ( $B_s$ ), estimated by dilatometry, was almost identical for all steels, i.e.  $500 \pm 5 \text{ °C}$ . Upon modifying the Si:Al ratios (3:1, 1:1 and 1:3), the measured martensitic transformation start temperature ( $M_s$ ) increased from 240 to 253 °C. The experimental values of the  $M_s$  temperatures

$$\text{wt.}\%C = \frac{\lambda_{k\alpha}}{2 \sin \theta} \times \sqrt{8 - 3.572 - 0.0012 \text{wt.}\%Mn + 0.00157 \text{wt.}\%Si - 0.0056 \text{wt.}\%Al} \\ 0.033$$

were in good agreement with the ones calculated using the empirical formula, proposed by Mahieu et al. [42]. Specimens for tensile tests (ASTM E8 standard) were prepared from the quarter through-thickness position of austempered sheets. Flat tensile samples were prepared parallel to the rolling direction. The tensile tests were done using an universal Instron 8861 testing machine with a 100 kN load cell operated at a constant strain rate of  $1 \times 10^{-3} \text{ s}^{-1}$  at room temperature. The yield strength (YS) was taken as 0.2% offset stress ( $\sigma_{0.2}$ ). The data points are averages from three tests. The impact toughness was measured on normalized Charpy V-notched samples of  $10 \times 10 \text{ mm}^2$  from  $-60$  to  $100 \text{ °C}$  using a 500 J tester (Tinius Olsen, FAHC-J-500-01) according to the standard BS EN 10 045-1: 1990. The systematic errors of the absorbed energy for the Charpy tests at 20, 40 and  $100 \text{ °C}$  were estimated as  $\pm 4$ ,  $\pm 7$  and  $\pm 15 \text{ J cm}^{-2}$ , respectively.

The  $\gamma_R$  volume fractions were determined by optical microscopy (OM) in conjunction with tinted color etching (TCE), electron back-scattered diffraction (EBSD) and X-ray diffraction (XRD). TCE was applied using a mixture of sodium metabisulfite ( $1 \text{ g Na}_2\text{S}_2\text{O}_5 \cdot \text{H}_2\text{O} + 100 \text{ ml dis-}$

tilled  $\text{H}_2\text{O}$ ) and picric acid (4%). In order to inhibit the deformation-induced transformation of  $\gamma_R$  into  $\alpha'$ -martensite during mechanical polishing, all specimens for XRD and EBSD measurements were prepared using electropolishing and chemical etching (Lectropol-5, Struers™) with a solution of acetic acid (90 vol.%) and perchloric acid (10 vol.%). All EBSD phase maps were acquired using a step size of 50 nm and post-processed using the TSL-OIM software. A confidence index (CI) value above 0.15 for phase identification was used [43,44]. Average phase fractions and distribution of  $\gamma_R$  were determined via EBSD using five or more data sets in each case. XRD measurements were done at 40 kV and 20 mA using Cu  $K_\alpha$  radiation. Integrated intensities of the  $(200)_\alpha$ ,  $(211)_\alpha$ ,  $(220)_\gamma$ ,  $(311)_\gamma$  Bragg peaks were determined for the calculation of the  $\gamma_R$  fractions [45]. Thermodynamic calculations were performed using Thermo-Calc [46], using a database for the Fe–Mn–Al–C quaternary system [47]. TEM samples were prepared by mechanical polishing of thin foils down to a thickness of less than 100  $\mu\text{m}$  followed by jet-polishing in a Tenupol-5 (Struers™), using a chemical solution of 90%  $\text{CH}_3\text{COOH}$  and 10%  $\text{HClO}_4$ . TEM Bright-field images and selected-area diffraction patterns were obtained with a JEOL 2010F microscope operated at 200 kV. The average C content in the  $\gamma_R$  phase was investigated by XRD and APT. From XRD, the C content in  $\gamma_R$  was determined as a function of the alloying elements according to [48]:

where  $\theta$  and  $\lambda_{k\alpha}$  represent the angle of the  $(220)_\gamma$  plane and the wavelength of the X-ray Cu target. Specimens for APT analyses were fabricated using a dual-beam focused ion beam (FIB) (FEI, Helios Nano-Lab 600) [49,50]. APT was performed on a laser-assisted wide-angle tomographic atom probe (LAWATAP™, CAMECA) equipped with a pulsed laser (525 nm wavelength,  $\sim 130 \text{ fs}$  pulse width). Measurements were performed at a tip temperature of 50 K using laser pulses of  $\sim 0.5 \text{ nJ}$  pulse energy,  $\sim 80 \mu\text{m}$  beam diameter and 100 kHz pulse repetition rate [22,23].

### 3. Results

#### 3.1. Mechanical properties

##### 3.1.1. Tensile tests

Fig. 2 shows values for the ultimate tensile strength (UTS), yield strength (YS), and uniform elongation (UE) of the steels. The mechanical properties vary significantly with the austempering temperature. In the 31SB-TRIP alloy (Si:Al = 3:1), the YS and UE drop from 706 MPa and 41% down to 585 MPa and 10%, respectively, with increasing the austempering temperature, while the UTS

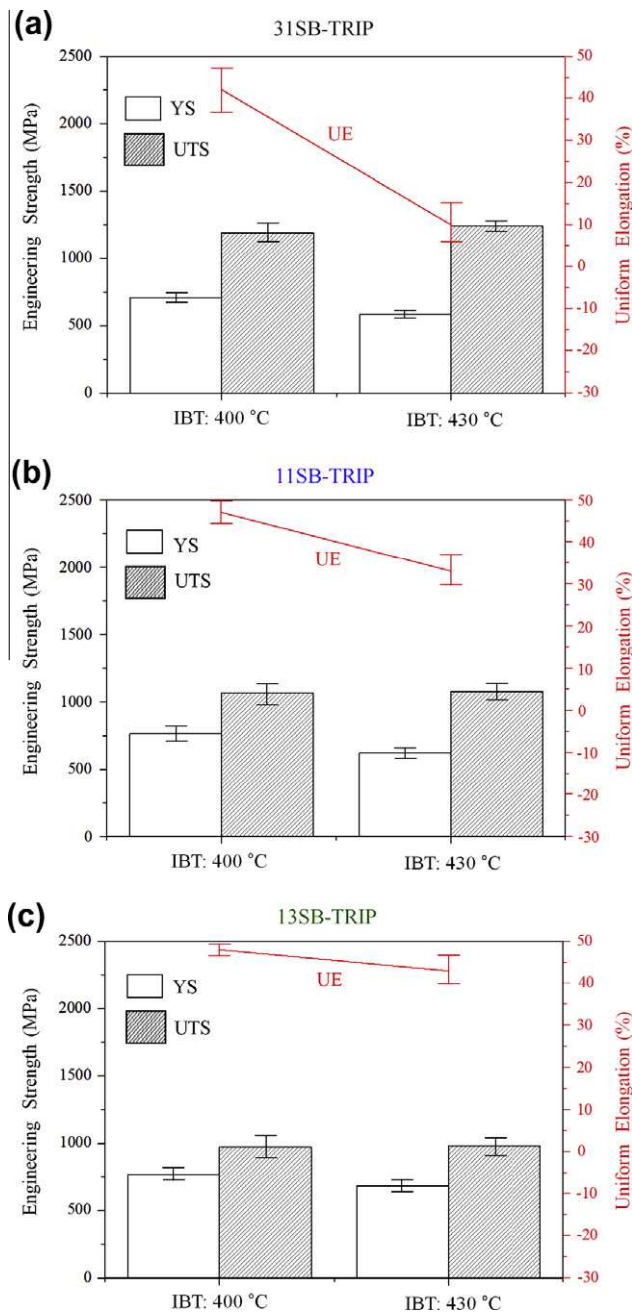


Fig. 2. Mechanical properties for varying austempering temperatures and Si:Al ratios: (a) 31SB-TRIP steel (Si:Al ratio = 3:1), (b) 11SB-TRIP steel (Si:Al ratio = 1:1) and (c) 13SB-TRIP steel (Si:Al ratio = 1:3). YS, yield strength; UTS, ultimate tensile strength; UE, uniform elongation.

increases from 1191 to 1242 MPa (Fig. 2a). The mechanical properties of the steels depend on the Si:Al ratio. Reducing the Si:Al ratio from 3:1 to 1:3 causes the YS and UE to increase from 706 MPa and 41% to 772 MPa and 49% (austempering at 400 °C), whereas the UTS decreases from 1191 to 973 MPa. Surprisingly, the austempering temperature does not significantly affect the mechanical properties of the 13SB-TRIP (Si:Al = 1:3) steel (Fig. 2c). The mechanical results suggest that the balance between strength and elongation is controlled by both the Si:Al ratio and the austempering temperature.

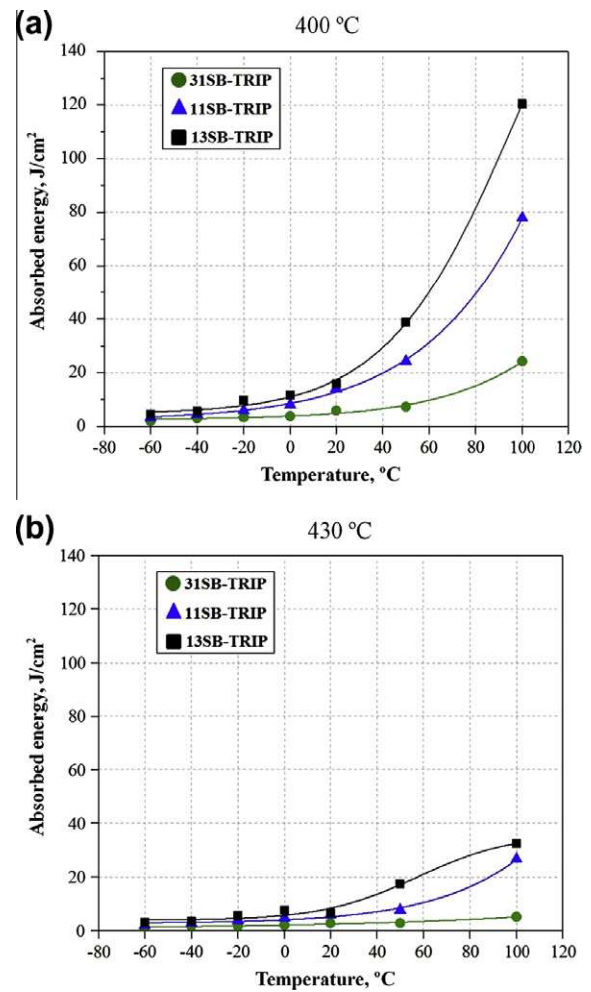


Fig. 3. Charpy impact test results for the 31SB-TRIP (Si:Al ratio = 3:1), 11SB-TRIP (Si:Al ratio = 1:1), and 13SB-TRIP (Si:Al ratio = 1:3) steels, austempered at (a) 400 °C and (b) 430 °C.

### 3.1.2. Charpy impact tests

Fig. 3 shows the impact toughness vs. temperature for all steels. The toughness of all three alloys is almost identical and relatively low below 20 °C, due to their high C concentration and brittle behavior. Above 50 °C, the absorbed energy of all alloys increases (ductile regime). A remarkable increase in impact toughness at high temperatures is observed for the 13SB-TRIP (Si:Al = 1:3) steel austempered at 400 °C, while the 31SB-TRIP (Si:Al = 3:1) steel only absorbs up to 24 J cm<sup>-2</sup> (Fig. 3a). When austempered at 430 °C, the 13SB-TRIP steel also exhibits higher toughness than the other steels, even though the total absorbed energy remains lower than for the same steel austempered at 400 °C (Fig. 3b). This shows that both the Si:Al ratio and the austempering temperature play a significant role for the toughness at high temperatures.

## 3.2. Microstructural characterization

### 3.2.1. Volume fraction of retained austenite

Fig. 4 shows the microstructure as observed by OM in conjunction with the TCE. The  $\alpha_B$  and  $\gamma_R$  phases appear



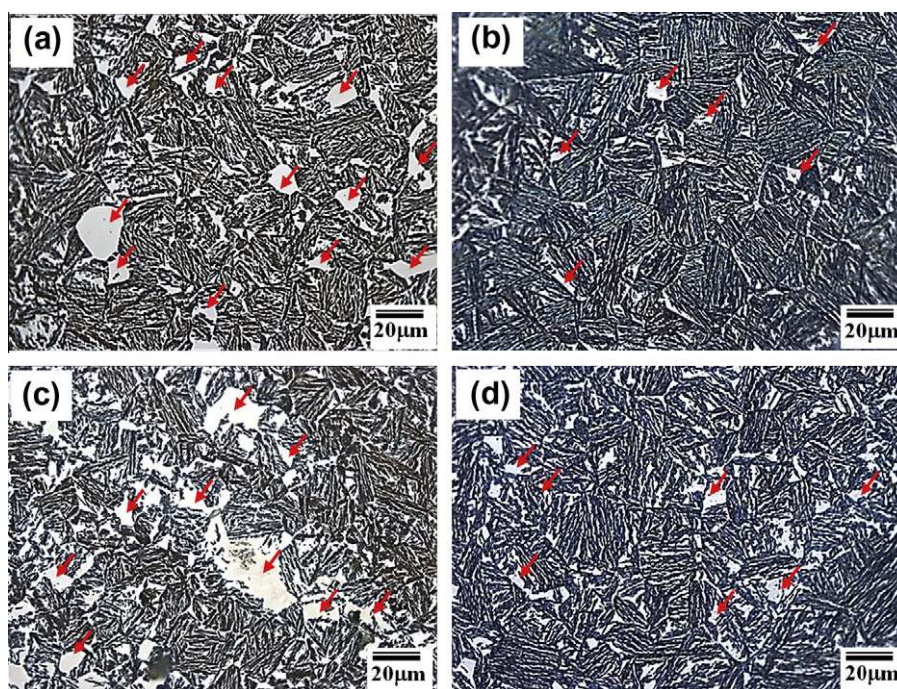


Fig. 4. Microstructure as observed by OM using the tinted color etching method (a) 31SB-TRIP (Si:Al ratio = 3:1) and (b) 13SB-TRIP (Si:Al ratio = 1:3) steels austempered at 400 °C, and (c) 31SB-TRIP and (d) 13SB-TRIP steels austempered at 430 °C (blue and brown, bainitic ferrite; white, retained austenite; red arrows, blocky-type austenite). (For interpretation of the references to colour in this figure legend, the reader is referred to the web version of this article.)

as blue or brown and white, respectively. All steels have a typical upper bainitic microstructure with partial transformation of austenite to bainite, leading to a bainitic–austenitic microstructure ( $\alpha_B$  and  $\gamma_R$ ). Two types of  $\gamma_R$  phases can be distinguished. One is characterized by isolated  $\gamma_R$  pools and the other one occurs with a fine film- or lath-type morphology of  $\gamma_R$  surrounded by  $\alpha_B$ . These  $\gamma_R$  morphologies are referred to as blocky-type  $\gamma_R$  and film-type  $\gamma_R$ , respectively. The distribution of coarse blocky-type  $\gamma_R$  is inhomogeneous, more specific, it is mainly dispersed along the prior austenite grain boundaries (indicated by red arrows in Fig. 4). The volume fraction of metastable  $\gamma_R$ ,  $V(\gamma_R)$ , increases with increasing austempering temperature and Si:Al ratio. In particular, the grain size of blocky-type  $\gamma_R$  decreases upon lowering the Si:Al ratio from 3:1 to 1:3 and upon a temperature drop from 430 to 400 °C. More details about the constituent phases were observed by EBSD. Fig. 5 shows the area fraction and distribution of  $\alpha_B$  and  $\gamma_R$  in the 31SB-TRIP and 11SB-TRIP steels, austempered at 400 °C as observed via EBSD phase maps and inverse pole figure (IPF) maps of  $\gamma_R$ .  $\alpha_B$  and  $\gamma_R$  are identified as red and green in the phase maps, respectively. The black arrows indicate blocky-type  $\gamma_R$  distributed at the prior austenite grain boundaries, as observed from the IPF maps of  $\gamma_R$  (see Fig. 5). The EBSD maps confirm that the microstructure of the investigated steels consists of  $\alpha_B$  and  $\gamma_R$  without carbide precipitates and  $\alpha'$ -martensite. Also, the EBSD data show a larger fraction of  $\gamma_R$  (34.5 vol.%) in the 31SB-TRIP steel as compared to the 11SB-TRIP sample

(30.7 vol.%). The size of blocky-type  $\gamma_R$  decreases with increasing the fraction of film-type  $\gamma_R$  upon lowering the Si:Al ratio from 3:1 to 1:1, in agreement with the results obtained from OM (Fig. 4).

The  $V(\gamma_R)$  values (volume fractions), including both blocky- and film-type  $\gamma_R$ , determined from OM, EBSD and XRD for the different alloys, are plotted in Fig. 6. OM yields the highest value for  $V(\gamma_R)$ , although most of the  $\gamma_R$  grains were of submicrometer size. There are two reasons for this observation. (i) It could be due to the inhomogeneous distribution of coarse blocky-type  $\gamma_R$ . OM has the largest field of view among the applied techniques and is hence able to map a large fraction of coarse blocky-type  $\gamma_R$ . The average value of  $V(\gamma_R)$  measured by OM is, hence, overestimated. (ii) It could be due to the limited resolution of OM regarding the irregular morphology of blocky- and film-type  $\gamma_R$  in the present steels. The nanometer-scaled film-type  $\gamma_R$  cannot be resolved by OM and leads to an artificial spread of the  $\gamma_R/\alpha_B$  interface width. It is, therefore, plausible that the  $\alpha_B$  surrounding by film-type  $\gamma_R$  is regarded as  $\gamma_R$  when measuring the overall  $V(\gamma_R)$  values.

In this context the overall volume fraction  $V(\gamma_R)$  as determined by EBSD is consistent with the XRD data (see Fig. 6) taking into account the corresponding resolution limits and the limited size of the area of the EBSD maps analyzed. According to Tirumalasetty et al. [51], the deviation between EBSD and XRD data for  $V(\gamma_R)$  in conventional TRIP steels can also be explained by the differences in penetration depths for EBSD and XRD, which



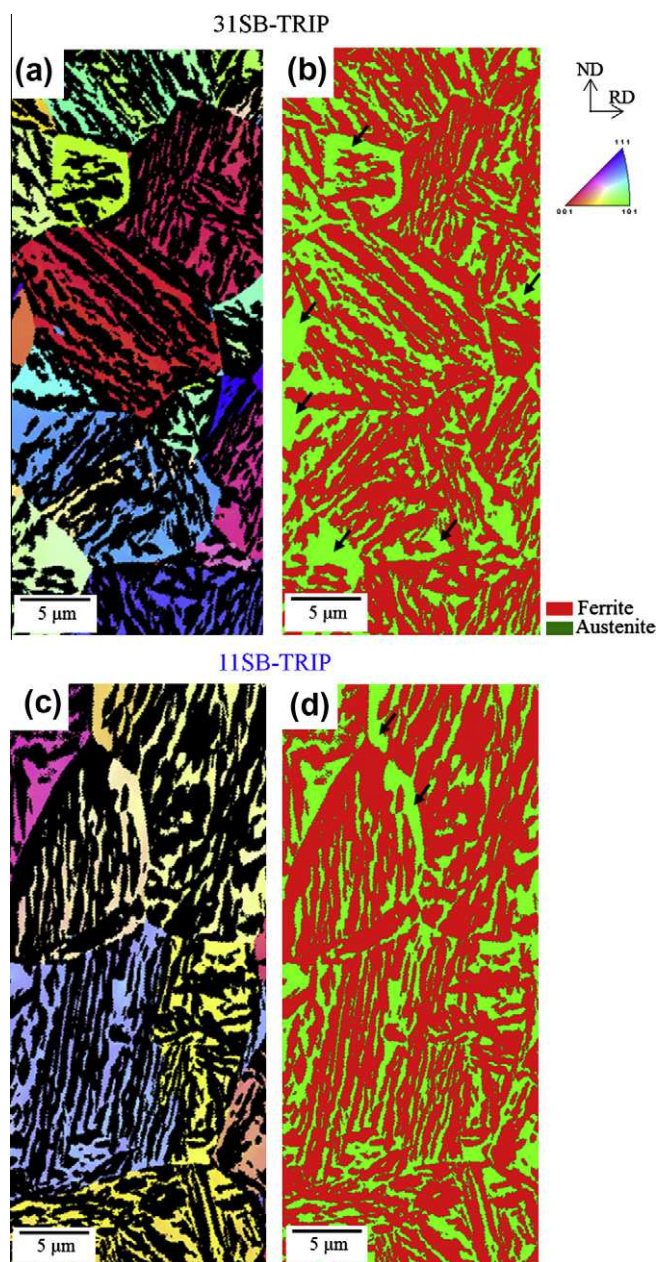


Fig. 5. (a) Electron back scattered diffraction (EBSD) inverted pole figure (IPF) map of austenite and (b) phase map for 31SB-TRIP (Si:Al ratio = 3:1), and (c) IPF map of austenite and (d) phase map for 11SB-TRIP (Si:Al ratio = 1:1) steel, austempered at 400 °C (red, bainitic ferrite; green, retained austenite; black arrows, blocky-type austenite). (For interpretation of the references to colour in this figure legend, the reader is referred to the web version of this article.)

are approximately 50 nm and 11 μm, respectively. Hence, EBSD generally is a more surface-sensitive analysis compared to XRD. To overcome the limits associated with the relatively small analyzed area of each individual EBSD map, the  $V(\gamma_R)$  values obtained from EBSD were averaged over a total of five or more data sets. Although the absolute  $V(\gamma_R)$  values of OM show some deviations from the EBSD and XRD results, as discussed above, the relative trends in

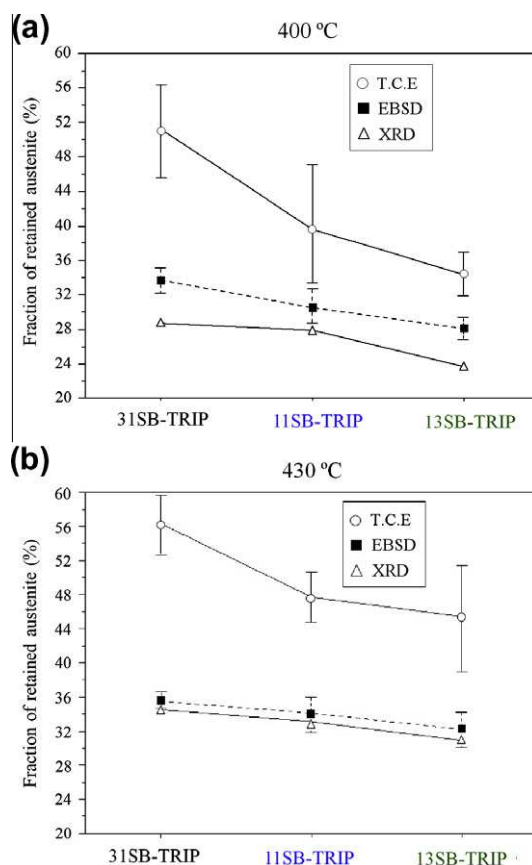


Fig. 6. Volume fraction of retained austenite in the steels determined by OM, XRD and EBSD. SB-TRIP steels austempered at (a) 400 °C and (b) 430 °C.

the change in  $V(\gamma_R)$  depending on the Si:Al ratio and austempering temperature are nonetheless similar. For an accurate estimation of the overall  $V(\gamma_R)$  value, we considered the values obtained from XRD and EBSD in this study.

An increase in the Si:Al ratio from 1:3 to 3:1 leads to a slight increase in the overall  $V(\gamma_R)$  for the steels annealed at either 400 °C (Fig. 6a) or 430 °C (Fig. 6a), respectively, for 160 min. As the driving force for the bainitic transformation increases with higher Al content, the  $V(\gamma_R)$  in the SB-TRIP steels is correspondingly reduced. Moreover, for all alloys a dependence of  $V(\gamma_R)$  on the austempering temperature is found. An increase in the austempering temperature leads to a higher  $V(\gamma_R)$  (from 29.6 vol.% at 400 °C to 34.4 vol.% at 430 °C in the 31SB-TRIP steel, and from 23.8 vol.% at 400 °C to 31.0 vol.% in the 13SB-TRIP steel). These results are in excellent agreement with previously reported experiments and calculations for Al-alloyed TRIP steels containing no Si [9–11]. We conclude that a lower Si:Al ratio (Si:Al = 1:3) and lower austempering temperature (400 °C) promote bainitic transformation. Note that, especially for the 13SB-TRIP steel, no significant correlation is observed between the overall  $V(\gamma_R)$  and the mechanical properties obtained for the different temperatures.

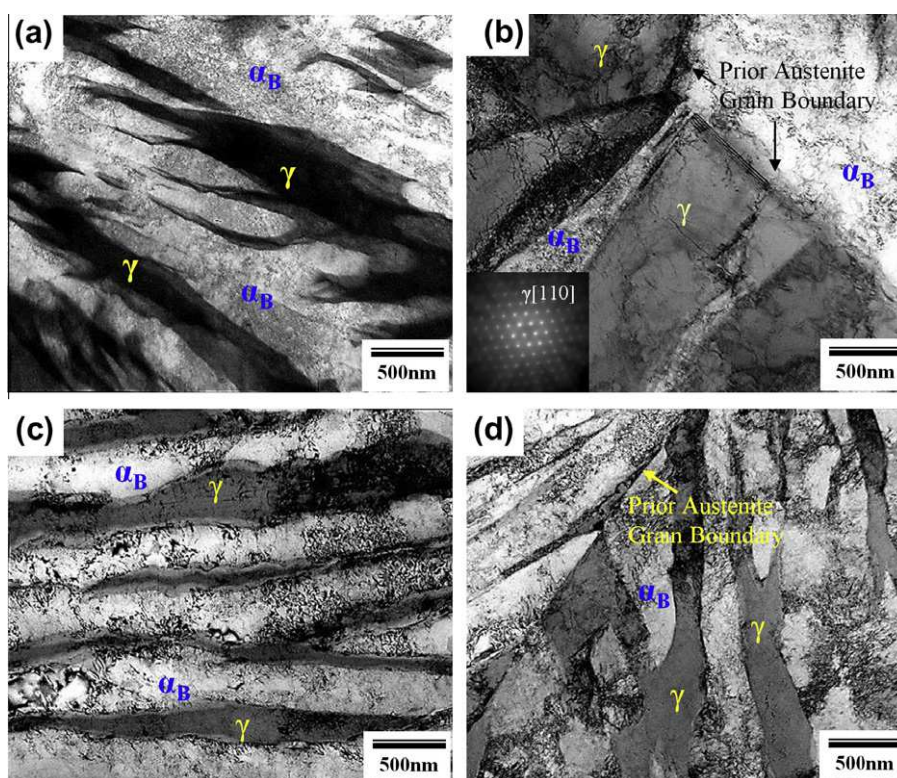


Fig. 7. TEM images of SB-TRIP steels ( $\gamma_R$ : retained austenite and  $\alpha_B$ : bainitic ferrite). 31SB-TRIP (Si:Al ratio = 3:1) austempered at (a) 400 °C and (b) 430 °C, and 13SB-TRIP (Si:Al ratio = 1:3) austempered at (c) 400 °C and (d) 430 °C.

### 3.2.2. Morphology of retained austenite observed by TEM

Besides the volume fraction, the morphology of  $\gamma_R$  also plays an important role on the elongation and UTS of the SB-TRIP steels [17,18]. Fig. 7 shows TEM images of the 31SB-TRIP and 13SB-TRIP steels, austempered at 400 and 430 °C, respectively. The TEM micrographs and corresponding diffraction pattern reveal a typical upper bainitic–austenitic microstructure consisting of a mixture of  $\alpha_B$  (white contrast) and film-type  $\gamma_R$  (dark contrast), but no cementite, in good agreement with the EBSD results. Thus, there is no microstructural evidence for the decomposition of  $\gamma_R$  into  $\alpha_B$  and carbides. We found that the average width of the  $\alpha_B$  plate increases from  $350 \pm 18$  nm to  $430 \pm 30$  nm upon increasing the austempering temperature for the 13SB-TRIP steel. The fine film-type  $\gamma_R$  (having a sheave-shaped morphology) is found to be distributed along the plate boundaries, while the blocky-type  $\gamma_R$  is mainly distributed at the prior austenite grain boundaries (Fig. 7). This observation is in accordance with the EBSD data (Fig. 5).

### 3.2.3. Analysis of alloying elements in retained austenite by atom probe tomography

Using APT, we investigated chemical gradients across  $\alpha_B/\gamma_R$  phase boundaries. Fig. 8a and b show a 3-D map of C and a local composition profile across  $\alpha_B/\gamma_R$  phase boundary (along the white arrow in Fig. 8a) in a 31SB-TRIP sample austempered at 400 °C. The distribution of

C in the analyzed volume of  $34 \times 34 \times 115$  nm<sup>3</sup> is not uniform, i.e. C-enriched and depleted regions can be clearly distinguished (see Fig. 8a). These zones are identified as  $\gamma_R$  and  $\alpha_B$ , respectively, by their characteristic C content (Fig. 8b). The C concentrations in  $\gamma_R$  and  $\alpha_B$  are  $5.38 \pm 0.39$  at.% and  $0.44 \pm 0.42$  at.%, respectively. Thus, there is no accumulation of C at the interface, indicating that the phase boundary does not act as a sink for C [19]. We also studied the contents of Si, Mn and Al using the local composition profiles with the volume of  $15 \times 15 \times 25$  nm<sup>3</sup> (Fig. 8b). The Si content in  $\alpha_B$  and  $\gamma_R$  is  $3.05 \pm 0.28$  at.% and  $2.76 \pm 0.24$  at.%, while the Mn content amounts to  $0.87 \pm 0.33$  at.% and  $1.10 \pm 0.30$  at.% in  $\alpha_B$  and  $\gamma_R$ , respectively. Si and Mn atoms are negligibly partitioned to the constituent phases considering statistical errors. Interestingly, remarkable concentration spikes of Si and Mn occur at the  $\gamma_R/\alpha_B$  interface, and reach a level of 4.47 at.% (2.4 wt.%) for Si and 2.01 at.% (1.9 wt.%) for Mn, which are beyond the limits of the  $\pm 2\sigma$  interval. Therefore, on this statistical basis, these fluctuations can be regarded as real effects related to the redistribution of Si and Mn atoms during  $\gamma$ -to- $\alpha_B$  transformation.

Additionally, no clear Al peak appears in the local profiles (Fig. 8b), although the global Al concentration is 0.5 wt.% (0.99 at.%) in the 31SB-TRIP alloy. It could be due to the limited sampling volume sizes used for local profiles. There are considerable overlaps of the  $^{27}\text{Al}^+$  peak and  $^{54}\text{Fe}^{2+}$  peak at 27 Da in the mass spectrum. Taking into



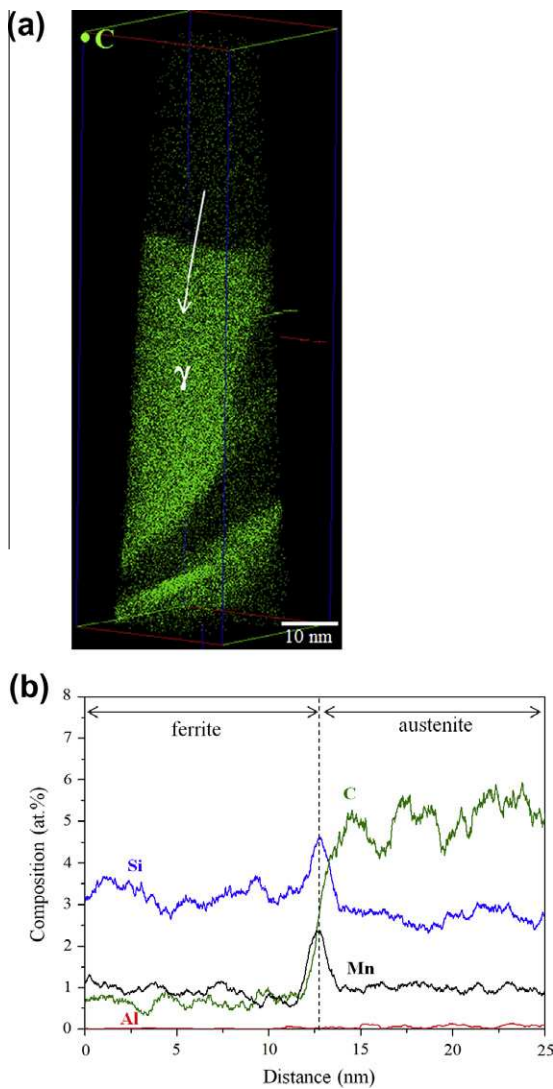


Fig. 8. (a) C atom map and (b) corresponding C, Mn, Si and Al concentration profiles (along the arrow) across the  $\alpha_B/\gamma_R$  phase boundary in the 31SB-TRIP (Si:Al ratio = 3:1) steels austempered at 400 °C.

account the isotope ratios of Fe, we could estimate that the contributions of  $^{54}\text{Fe}^{2+}$  and  $^{27}\text{Al}^+$  to the peak at 27 Da are about 62% and 38%, respectively. As we assigned the peak at 27 Da to  $^{54}\text{Fe}^{2+}$ , the Al concentration is hence underestimated in the local composition profiles. The overall Al content could be nonetheless precisely corrected by applying a deconvolution procedure for the overlapping mass peaks [52]. As a result, the average measured Al content is estimated as  $1.08 \pm 0.19$  at.%, which corresponds well to the nominal composition of the alloy.

The reconstructed APT map of an 11SB-TRIP sample austempered at 400 °C also shows three distinct regions with different C content, namely  $\gamma_R$ , carbides, and  $\alpha_B$  (follow regions from top to bottom in Fig. 9a). Fig. 9b and c show the corresponding concentration profiles perpendicular to the interface without and with the carbide, respectively. The Si content in  $\alpha_B$  and  $\gamma_R$  is  $2.35 \pm 0.25$  at.% and  $2.59 \pm 0.30$  at.%, while the Mn content amounts to  $1.27 \pm 0.31$  at.% and  $1.42 \pm 0.26$  at.% in  $\alpha_B$  and  $\gamma_R$ , respec-

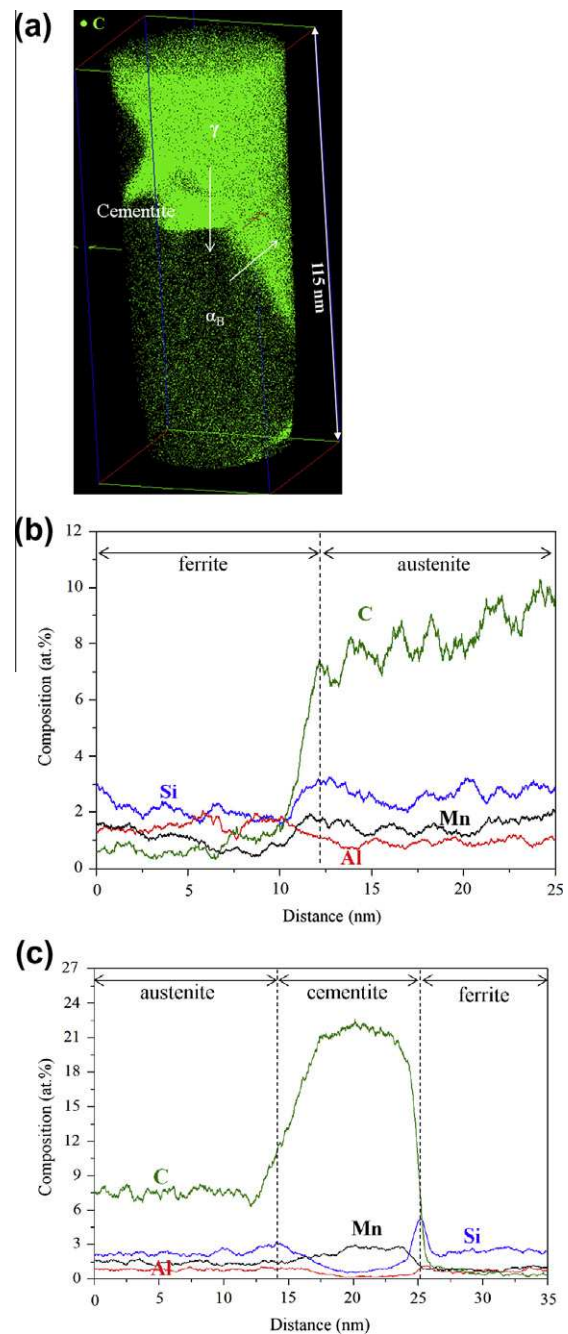


Fig. 9. (a) C atom map; (b) local distribution of alloying elements; (c) corresponding C, Al, Si and Mn concentration profiles across the phase boundaries of austenite, cementite and ferrite in the 11SB-TRIP (Si:Al ratio = 1:1) steel sample austempered at 400 °C.

tively. Si and Mn atoms are negligibly partitioned to the phases considering statistical errors. However, small Si and Mn concentration peaks are observed at the  $\gamma_R/\alpha_B$  interface (see Fig. 9b). The concentrations of Si and Mn at the  $\gamma_R/\alpha_B$  interface are measured as 3.1 and 1.9 at.%, respectively. Nevertheless, their peak amplitudes at the  $\gamma_R/\alpha_B$  interface are within the limits of the  $\pm 2\sigma$ , compared with their average signals. Consequently, these fluctuations cannot be regarded as real spikes.



On the other hand, the C concentrations in the  $\gamma_R$  and  $\alpha_B$  are  $7.52 \pm 0.40$  at.% and  $0.24 \pm 0.04$  at.%, respectively. The C content in the carbide suggests that it could be a nanosized cementite precipitate which formed at the  $\gamma_R/\alpha_B$  interface during upper bainite transformation. It does not seem to correspond to one of the well-known transition carbides such as  $\varepsilon\text{-Fe}_2\text{C}$ ,  $\eta\text{-Fe}_2\text{C}$ ,  $\chi\text{-Fe}_5\text{C}_2$ , and  $\text{Fe}_7\text{C}_3$ . The deviation of the cementite concentration in the local profile, as measured by APT, from the exact  $\text{Fe}_3\text{C}$  stoichiometry could have the following reasons: Firstly, the C content inside the carbide can be underestimated by the inaccuracy in defining the mass-to-charge ratio of the  $\text{C}_2^+$  and  $\text{C}_4^+$  peaks. In this study, the C content was precisely corrected by applying the identification procedure of C peaks as proposed by Li et al. [53]. Following this procedure the C content inside the particles is  $23.85 \pm 0.33$  at.%, which slightly deviates from the exact  $\text{Fe}_3\text{C}$  stoichiometry. Secondly, the C content of cementite can continuously vary with its formation temperature due to the formation of C-vacancy pairs, as has been recently shown by neutron diffraction studies and ab initio calculations [26,54]. In upper bainite, the carbide precipitates as a secondary process [13–19]. This indicates that the cementite observed in this alloy is formed at a relatively low temperature below  $500^\circ\text{C}$  ( $B_s$  temperature). It is, hence, plausible that the composition of cementite as detected by APT is slightly below 25 at.% due to its low formation temperature. Another possible explanation would be related to the interaction between C molecule ions and the APT laser pulses. Laser pulsing can at worst lead to composition errors that depend on the laser energy such as preferential evaporation, elemental surface diffusion and local magnification [55–57]. These effects possibly account for a slight difference in the C content inside cementite particles but are still subjects of ongoing research [52,57,58].

For the SB-TRIP steels, we have not been able to detect nanosized cementite precipitates by EBSD and TEM measurements due to the EBSD resolution limits as well as due to the insufficient TEM contrast between the neighboring  $\gamma_R$  grains. Only by using APT can we confirm and resolve the local precipitation of nanometer-sized cementite at the  $\gamma_R/\alpha_B$  interface in upper bainite. The APT result further shows that upper  $\alpha_B$  itself is devoid of precipitates [13]. It is also revealed that Si and Al atoms are depleted inside the cementite due to their low solubility, while Mn is enriched. The concentration of substitutional elements, such as Si, Al and Mn, fluctuates at the  $\gamma_R$ /cementite as well as at the cementite/ $\alpha_B$  interface (Fig. 9c). No enrichment of either Si or Mn can be observed at the  $\gamma_R$ /cementite interface, whereas remarkable accumulations of Al and in particular Si are detected in the vicinity of the cementite/ $\alpha_B$  interface.

Fig. 10a and b show a 3-D map of C atoms and a composition profile of a 13SB-TRIP steel sample austempered at  $400^\circ\text{C}$ . The C distribution in the analyzed volume ( $38 \times 38 \times 82 \text{ nm}^3$ ) is not uniform. The composition profile in Fig. 10b indicates that the C content in  $\gamma_R$  and  $\alpha_B$  is

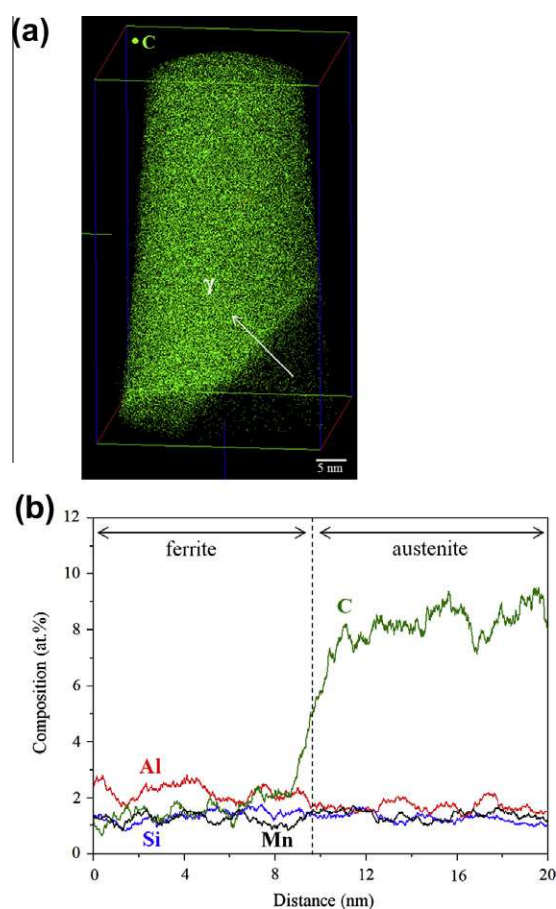


Fig. 10. (a) C atom map and (b) corresponding C, Mn, Si and Al concentration profiles (along the arrow) across the  $\alpha_B/\gamma_R$  phase boundary in the 13SB-TRIP (Si:Al ratio = 1:3) steels austempered at  $400^\circ\text{C}$ .

$9.18 \pm 0.4$  at.% and  $<1$  at.%, respectively. The concentrations of Si, Mn and Al were identical in both phases considering their statistical errors. There is also no significant redistribution of Al, Si and Mn atoms across the  $\gamma_R/\alpha_B$  interface in the 13SB-TRIP steel.

Fig. 11a and b present the C concentration (in wt.%) in  $\gamma_R$  as determined from XRD and APT analyses, respectively. The data reveal that the C content in  $\gamma_R$  increases with decreasing the Si:Al ratio from 3:1 to 1:3, where the change in the C content differs with different austempering temperature. The C content in  $\alpha_B$  as measured by APT is shown in Fig. 11c. The C concentration values together with the corresponding statistical errors were determined from several APT data sets. The current APT results clearly show that the C content in  $\gamma_R$  is affected by the austempering temperature as well as by the Si:Al ratio (see Fig. 11b). The deviation between the XRD and APT data can be explained by the fact that the C content in  $\gamma_R$  was determined by XRD under the simplified assumption that neither cementite formation nor C segregation at dislocations takes place. In addition, the C content in  $\alpha_B$  varies with the Si:Al ratio and the austempering temperature (Fig. 11c). The C content in  $\alpha_B$  is significantly higher than expected from PE, indicating that  $\alpha_B$  can also be supersat-

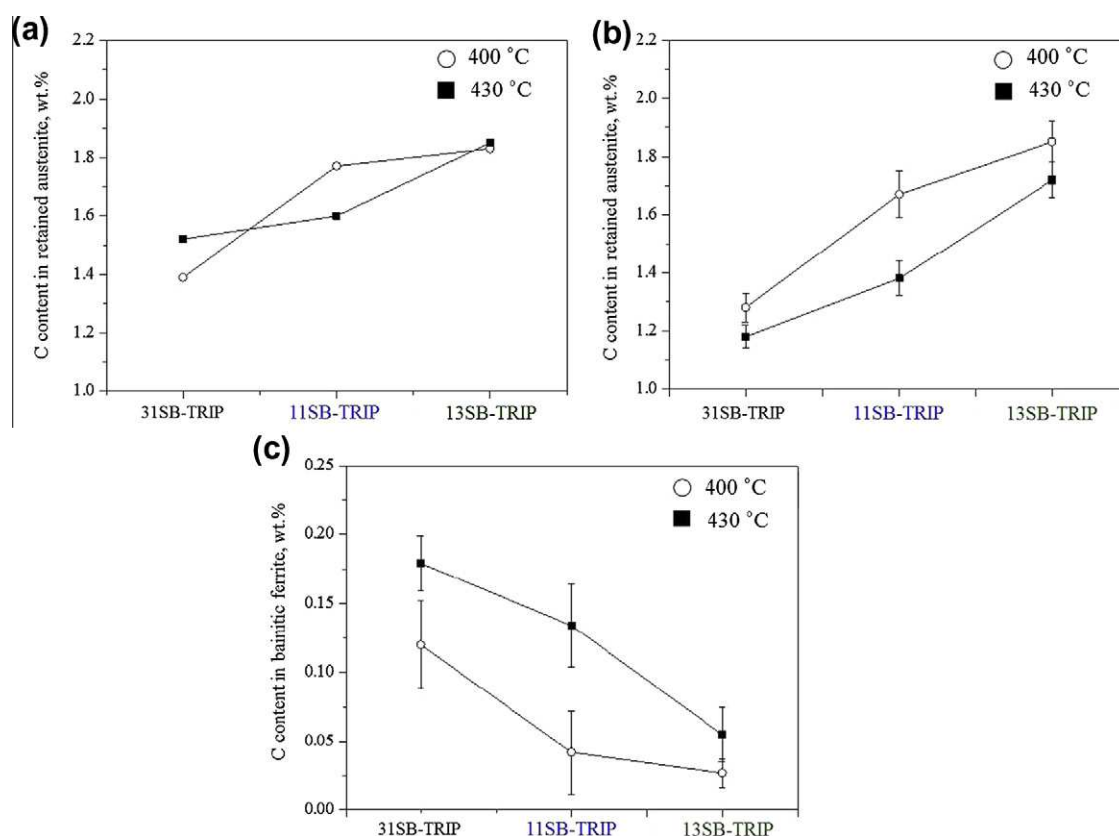


Fig. 11. Comparison of carbon content (wt.%) in retained austenite between (a) XRD measurements and (b) APT for varying austempering temperatures and the Si:Al ratios. (c) Estimated carbon content (wt.%) in bainitic ferrite by APT.

urated with C. These APT results are in agreement with previous reports [25].

### 3.2.4. Thermodynamic calculations

Fig. 12 shows the equilibrium volume fractions of the constituent phases as a function of the Si:Al ratio. The calculated diagrams confirm that the resulting microstructure consists of ferrite, austenite and a small fraction of cementite. Furthermore, it is revealed that the  $A_{e1}$  and  $A_{e3}$  temperatures are controlled by the Si:Al ratio. A decrease in the Si:Al ratio (from Si:Al = 3:1 to Si:Al = 1:3) leads to an increase in the  $A_{e1}$  temperature from 730 to 765 °C, and to a strong increase in the  $A_{e3}$  from 760 to 865 °C. As a result, a higher volume fraction of ferrite is observed for a lower Si:Al ratio, i.e. Al acts as a more effective ferrite former than Si and also indirectly as an austenite stabilizer due to its effect on rejecting C from ferrite into austenite. A low Si:Al ratio of 1:3 leads to an increase in the equilibrium ferrite fraction. This means that Al rather than Si accelerates bainitic ferrite transformation, in good agreement with the experimental results obtained by XRD and EBSD. Therefore, we anticipate that the  $\gamma_R$  in the 13SB-TRIP steels contains higher C contents, and hence is more stabilized, compared to the 31SB-TRIP steel. We also observe that as the Si:Al ratio drops from 3:1 to 1:3, the onset temperature for cementite formation increases in this quaternary system. We conclude from the calculations that the

barrier for cementite nucleation is more effectively reduced by Si than by Al, in good agreement with the APT experiment (Fig. 9c).

## 4. Discussion

### 4.1. Correlation between microstructure and mechanical properties

The microstructural characterization of the three steels provides an access to understanding their mechanical behavior. The strength and yield behavior of the alloys strongly depend on the grain size of the  $\alpha_B$ -plates, which determines the mean free path for dislocation glide [16]. Using TEM, we found that an increase in the austempering temperature leads to an increase in the  $\alpha_B$  plate width. This is due to a reduced nucleation rate of  $\alpha_B$  induced by a higher austempering temperature, resulting from a decrease in the driving force for bainite transformation. This suppression in the bainite transformation can lead to low dislocation density, low internal interface density and low internal stresses, which are induced by the shape changes associated with the  $\gamma$ -to- $\alpha_B$  transformation. Indeed, the dislocation density inside the  $\alpha_B$  plate, calculated by the integral width of the  $\{110\}$ ,  $\{200\}$  and  $\{211\}\alpha$  peaks in the XRD data [59], is about  $4.5 \times 10^{15}$  and  $1.7 \times 10^{15} \text{ m}^{-2}$  for the 31SB-TRIP steels annealed at 400 and 430 °C,



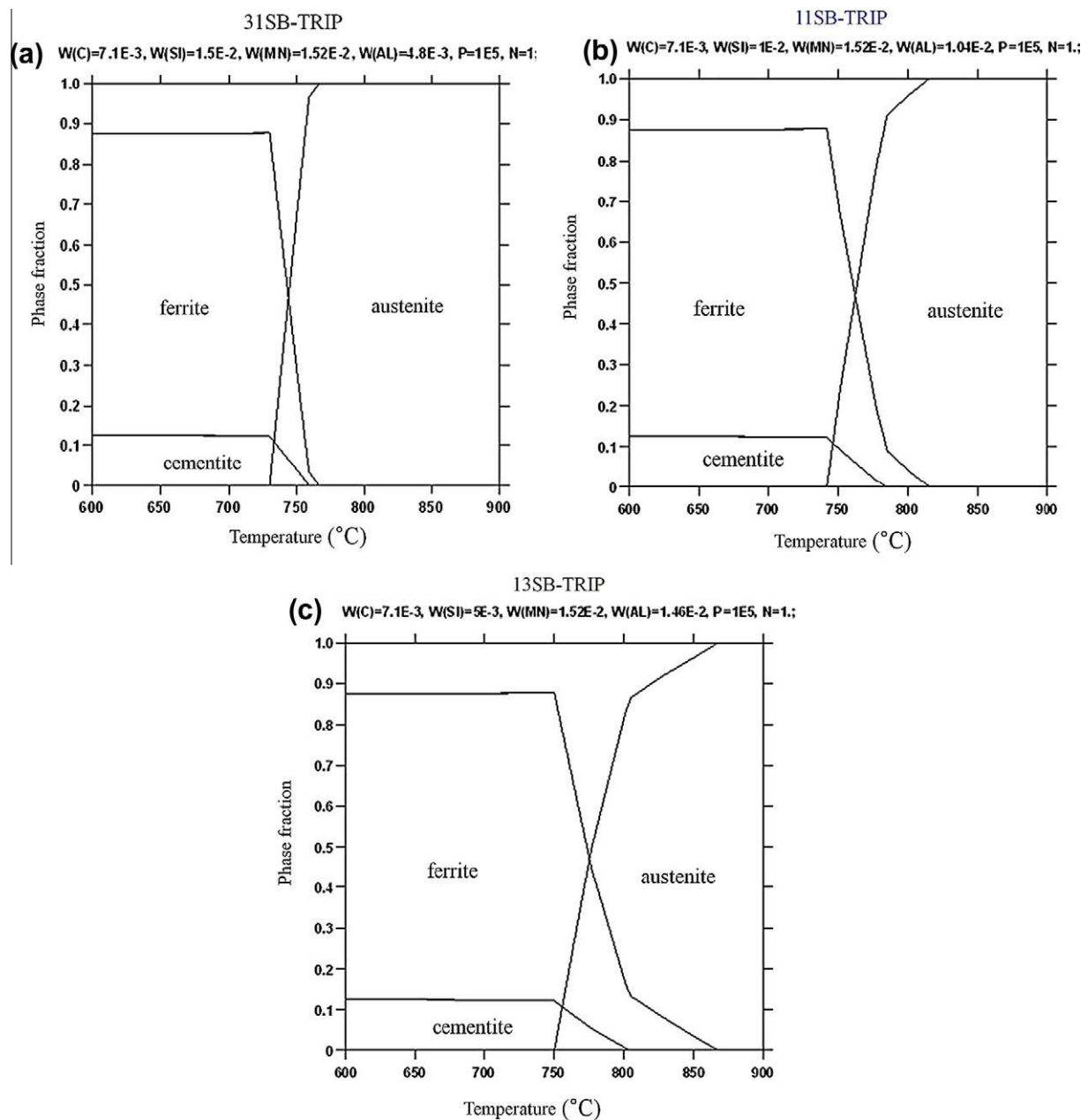


Fig. 12. Equilibrium volume fractions of the constituent phases for varying Si:Al ratios calculated using the software Thermo-Calc: (a) 31SB-TRIP (Si:Al ratio = 3:1), (b) 11SB-TRIP (Si:Al ratio = 1:1) and (c) 13SB-TRIP (Si:Al ratio = 1:3) steels.

respectively. The decrease in the relative trend of the dislocation density by higher annealing temperature was also reported elsewhere [60]. It is, therefore, recognized that the yield strength of the current alloys decreases with higher austempering temperature. The other factors contributing to strength and yielding behavior are the density of  $\gamma_R/\alpha_B$  interface dislocations and the  $\alpha_B$  plate width. However, these parameters do not explain the weak dependence of the mechanical properties in the 13SB-TRIP steels on the austempering temperature (Fig. 2c).

In this context we considered the  $\gamma_R$  phase to better understand the UTS behavior, since this phase substantially affects the strength. Three effects are important in this

context. (i) Transformation of metastable  $\gamma_R$  into hard martensite occurs during cooling to room temperature, thus increasing the strength. (ii) Upon mechanical loading, deformation-stimulated transformation of unstable  $\gamma_R$  into martensite occurs, thus increasing the strength via the TRIP effect [24–27]. The TRIP effect also enhances the strain-hardening rate and thus delays necking during tensile testing [15,61]. (iii) The morphology of the  $\gamma_R$  grains can also affect the strength during tensile loading. For instance, isolated pools of blocky-type  $\gamma_R$  which have a lower C content than film-type  $\gamma_R$  deteriorate elongation and UTS [16–18]. On the other hand, a fine film-type  $\gamma_R$  with higher C content (compared to blocky-type  $\gamma_R$ ) homo-

geneously aligns along the plate boundaries and hence can enhance the tensile strength.

As only a very low fraction of martensite has been observed upon cooling to room temperature in the SB-TRIP steels, it should not significantly contribute to strengthening. We observed that even though the overall volume fraction of  $\gamma_R$  slightly depends on the Si:Al ratio, a remarkable reduction in the grain size of blocky-type  $\gamma_R$  with increasing the film-type  $\gamma_R$  fraction is achieved through a lower Si:Al ratio. Therefore, taking into account a decrease in the UTS upon lowering the Si:Al ratio, we conclude that the contribution of  $\gamma_R$  to the UTS of the SB-TRIP steels in this study is mainly due to the TRIP effect during tensile loading. The solid solution strengthening effects contributing to the strength are discussed in more detail in the next section.

Since austenite is a ductile phase compared to bainitic ferrite, we expect its volume fraction to control the ductility of bainitic–austenitic TRIP steels [17]. However, surprisingly the ductility in the present alloys varies inversely with the measured overall  $\gamma_R$  fractions. In addition, varying the austempering temperature did not have a significant effect on the mechanical properties of the 13SB-TRIP alloy. This indicates that correlating ductility and  $\gamma_R$  fractions in these materials requires considering the mechanical, chemical, and thermal stability of  $\gamma_R$ .

So far, there are no clear explanations on the relationship between the impact toughness and the  $\gamma_R$  phase fraction in conventional TRIP steels. Specifically, we observe that the correlation between impact toughness and overall  $\gamma_R$  fraction, when sufficiently high to support a TRIP effect, is not linear. Even though the measured  $\gamma_R$  fractions are only slightly changed by the Si:Al ratio and the austempering temperature, a profound increase in the impact toughness of the SB-TRIP steels is found at elevated temperatures (20–100 °C), specifically for the 13SB-TRIP steel annealed at 400 °C (Fig. 3a). Other aspects, such as the dislocation density inside  $\alpha_B$  and the stabilization of  $\gamma_R$  upon loading, do not also fully account for such an enhanced toughness. As the time and temperature of impact tests are extremely limited and, respectively, low, the C atoms cannot diffuse from supersaturated  $\alpha_B$  into the  $\gamma_R$  during testing. In particular, C atoms are trapped at the dislocations within the  $\alpha_B$ . This means that the dislocation density within the  $\alpha_B$  does not affect the toughness value at temperatures below 100 °C (ductile regime). Furthermore, the low mobility of C within the  $\gamma_R$  makes it generally difficult to accelerate C diffusion inside the  $\gamma_R$  ( $\gamma_R$  stabilization) upon the loading. In this context the improved impact toughness is due to the thermal stability of  $\gamma_R$  in the as-quenched alloys, especially to both the size and local C content of  $\gamma_R$ . Considering the observation that the grain size of blocky-type  $\gamma_R$  with a relatively low C content was significantly influenced by changing the Si:Al ratio and the austempering temperature, we speculate that a higher fraction of fine film-type  $\gamma_R$  with lower fraction of coarse blocky-type  $\gamma_R$  is beneficial for the toughness.

Therefore, we suggest that the local C content of film-type  $\gamma_R$  and the grain size of blocky-type  $\gamma_R$  phase, which are influenced by the Si:Al ratio as well as by the austempering temperature, can be used to control its stability and thus its transformation kinetics into martensite via the TRIP effect during impact testing. Saha et al. [62] were indeed able to show that a toughness increase for a Fe–Ni–Cu–Cr alloy was due to the TRIP effect. Our current findings support this trend and further suggest that the optimized toughness observed for the 13SB-TRIP steel annealed at 400 °C for 160 min is due to the distribution and partitioning of C associated with morphological changes. However, blocky-type  $\gamma_R$ , observed from OM, EBSD and TEM, is not readily observed in APT without specific lift-out sample preparation methods, owing to the limited field of view of the analysis [60]. To quantitatively measure the C content of both blocky- and film-type  $\gamma_R$ , further experimental efforts are required.

The mechanical stability of metastable  $\gamma_R$  can be generally controlled by its size (constraining effect) [63], morphology [64], grain rotation [51] and C content [65] under tensile loading. Based on the Ludwigson–Berger [66] and Olson–Cohen models [67], the mechanical stability of  $\gamma_R$  in low C Mn–Si–Al TRIP steels austempered at 400 and 450 °C has been experimentally confirmed by measuring the magnetic saturation after tensile testing. Recent experimental approaches have been performed to reveal the deformation behavior of  $\gamma_R$  in TRIP steels [68–70]. According to previous results [61,71], a smaller  $\gamma_R$  grain size leads to a higher mechanical stability of  $\gamma_R$  due to effects related to the nucleation rate of martensite (constraining effect). As reported by Tirumalasetty et al. [51], the grain rotation of the  $\gamma_R$  grains having the highest Schmid factors during deformation results in a lowering of the Schmid factors, leading to a decrease in the critical resolved shear stress for martensitic transformation. Hence, the rotated  $\gamma_R$  grains, which are transformed into martensite at later stages of deformation, are also an additional factor contributing to the mechanical stability of  $\gamma_R$  for low-C TRIP steels [51]. For the present SB-TRIP steels, we find that a decreased grain size of blocky-type  $\gamma_R$  with increasing the fraction of film-type  $\gamma_R$  is achieved by lowering the Si:Al ratio and decreasing the austempering temperature. Blocky-type  $\gamma_R$  grains were found to be mechanically less stable and were transformed more easily during tensile loading, compared with lath-type or film-type  $\gamma_R$  grains [72]. Therefore, we confirm that the mechanical stability of metastable  $\gamma_R$  during tensile loading or toughness tests may significantly be controlled by the initial microstructure of  $\gamma_R$  grains, especially by the local C content in the  $\gamma_R$  associated with the grain size of blocky-type  $\gamma_R$ , as discussed above. As a consequence, the microstructure consisting of a smaller blocky  $\gamma_R$  and finer film-type  $\gamma_R$  in upper bainitic steels can improve the constraining effect exerted by the phases surrounding the  $\gamma_R$  phase or the  $\gamma_R$  grain rotation upon the deformation. This results in an increase of UTS, YS, elongation and toughness owing to



the higher mechanical stability of  $\gamma_R$ . Alternatively, these effects can be achieved by manipulating the Si:Al ratio and by reducing the austempering temperature from 430 to 400 °C.

#### 4.2. Effects of C partitioning on the stability of the $\gamma_R$ phase

We found that the austempering temperature and the Si:Al ratio are important parameters for controlling the mechanical stability and the initial microstructure of the  $\gamma_R$  phase.

The APT results show the C content in  $\gamma_R$  and  $\alpha_B$ , thus enabling us to understand the thermal stability of  $\gamma_R$  in the as-received steels as a function of the austempering temperature and the Si:Al ratio. We found that C rejection from supersaturated  $\alpha_B$  into  $\gamma_R$  is enhanced by a low Si:Al ratio of 1:3 and by a low austempering temperature of 400 °C. This leads to an improved chemical stabilization of  $\gamma_R$ , thereby suppressing the transformation of metastable  $\gamma_R$  into  $\alpha'$ -martensite at an early stage of straining. We propose that the integral mechanical properties as well as the impact toughness are controlled by the thermal stability of  $\gamma_R$  in the as-received steels.

Based on the microstructure evolution of  $\gamma_R$  and the partitioning of C, we generalized a mechanism for the transformation sequence occurring during thermal processing in this study. While the 31SB-TRIP steel, austempered at 430 °C, has a maximum  $\gamma_R$  volume fraction, the 13SB-TRIP steel, austempered at 400 °C, reaches the highest C content in  $\gamma_R$ . As discussed above, an optimum thermal stability of  $\gamma_R$  can be achieved with a low Si:Al ratio (Si:Al = 1:3) and a low austempering temperature (400 °C). Owing to an optimum thermal stability of  $\gamma_R$  in as-received samples, a weak dependence of the mechanical properties in the 13SB-TRIP (Si:Al = 1:3) steels on the austempering temperature is observed. Therefore, we propose that the 13SB-TRIP steels austempered at 400 °C exhibit the best combination of tensile properties and impact toughness.

On the other hand, higher Al content in the SB-TRIP steels is reported to increase the driving force for bainitic transformation [15]. Hence, a higher  $\alpha_B$  fraction and lower  $\gamma_R$  fraction (also smaller  $\gamma_R$  size) are found in the 13SB-TRIP steels during cooling to the austempering temperature as compared to the 31SB-TRIP steels, which results in an increased C content in  $\gamma_R$ . This effect is attributed to the rejection of C from  $\alpha_B$  into the neighboring  $\gamma_R$ . At a low austempering temperature, the transformation kinetics of austenite into bainite becomes slower, while the diffusion-controlled C gradient across the  $\gamma_R/\alpha_B$  boundary is evened out.

Additionally, we do not observe any C accumulation at the  $\gamma_R/\alpha_B$  interface in the three steels, as previously reported in Ref. [17]. This is ascribed to a diffusion-controlled transformation under local equilibrium rather than to an interface-controlled transformation [73,74]. Therefore, we observe no build-up of C concentration spike at

the  $\gamma_R/\alpha_B$  interface owing to the fact that C diffuses much faster inside the austenite than the substitutional atoms do, despite its strong affinity to Mn [75]. The C partitioning into austenite and the precipitation of carbides are known to be competitive processes [13,15]. Despite the presence of nanometer-sized cementite at the  $\gamma_R/\alpha_B$  interface in the steels containing a high content of Si + Al (Fig. 9), no significant trend is found for the C concentration in  $\gamma_R$  as a function of the transformation temperature and alloy chemistry. Hence, the present APT results support the suggestion by Caballero [17,19] that cementite precipitation is not a dominant process during upper bainite reaction in high-C TRIP steels.

#### 4.3. Substitutional partitioning and mechanisms of bainitic transformation in SB-TRIP steels

Using APT, we mapped the redistribution of Mn and Si atoms in the vicinity of the  $\gamma_R/\alpha_B$  interface in the 31SB-TRIP steels austempered at 400 °C (see Fig. 8b). The local magnification effect, a well-known reconstruction artifact of the APT technique, which is caused by a difference in the local evaporation field of the tip-shaped APT sample and which is particularly pronounced in heterogeneous materials, can lead to a blurred reconstruction of the interface region [76,77]. However, we did not detect any significant Si or Mn spikes at the  $\gamma_R/\alpha_B$  interfaces of the 11SB-TRIP and 13SB-TRIP steels (Figs. 9b and 10b), even though they had been analyzed under equivalent APT conditions as the 31SB-TRIP steel. Considering this point, the pronounced Si and Mn enrichments at the  $\gamma_R/\alpha_B$  interface of the 31SB-TRIP steel (Fig. 8b) is sufficiently pronounced to represent real effects, i.e. they are not APT reconstruction artifacts. The interface exhibiting Mn and Si concentration spikes may be a  $\gamma_R/\alpha_B$  phase boundary and not a prior austenite grain boundary. We assume this as no segregation of either C or other impurities, e.g. P and S, is visible at the interface. Therefore, our APT result confirms that some substitutional diffusion-controlled effects have indeed occurred in the 31SB-TRIP steel during the upper bainitic transformation, even though their spikes were monitored in a single APT data set and were not generally observed for all  $\gamma_R/\alpha_B$  interfaces. This experimental finding indicates that upper bainite transformation in the 31SB-TRIP steel can locally be controlled, at least to some extent, by a diffusional mechanism. This result is not in line with the work of Bhadeshia and Edmonds [13], who suggested that the incomplete bainite transformation (400 J mol<sup>-1</sup>) is controlled by a displacive mechanism.

Additionally, the current APT results reveal that Mn and Si spikes can occur on the heterointerface if the  $\alpha_B$  growth rate is slow enough, i.e. the order of the diffusivity of Mn and Si. In case that substitutional diffusion is involved in a local equilibrium mechanism, diffusion would be sluggish as the transformation kinetics would be controlled by substitutional diffusion according to a mixed-mode approach [24,73,78]. The accumulation of Mn and

Si at the boundaries between proeutectoid ferrite ( $\alpha$ ) and prior austenite ( $\gamma$ ) can lead to a solute drag effect as described by Lücke and Stüwe [79]. These drag effects associated with Si and Mn could even exceed the driving force for the  $\gamma$ -to- $\alpha$  transformation so that the ferrite transformation is kinetically blocked [37]. For a quaternary Fe–C–Mn–Si alloy this effect could occur already after about 1 s annealing time owing to the following enthalpy values involved, namely,  $\Delta G_{\text{drag}} = 200 \text{ J mol}^{-1}$  and  $\Delta G^{\gamma \rightarrow \alpha} = -181 \text{ J mol}^{-1}$  at  $700^\circ\text{C}$ . For the binding energies of Mn and Si in the vicinity of the as-quenched  $\gamma/\alpha$  interfaces we assumed  $E_{\text{Mn}} \sim -8 \text{ kJ mol}^{-1}$  and  $E_{\text{Si}} \sim -10 \text{ kJ mol}^{-1}$ , respectively. To better understand the accumulation of Mn at the boundaries, we used the flux equation for describing atomic jumps of Mn from the interface into the austenite, thereby building up the observed concentration spike [32]:

$$J_{\text{Mn}}^{I \rightarrow \gamma} = \frac{X_{\text{Mn}}^I \cdot M_{\text{Mn}}^{\text{Trans-int}}}{V_m} \cdot \frac{(\mu_{\text{Mn}}^\gamma - \mu_{\text{Mn}}^I)}{\delta} \times \left( 1 - \exp \left( \frac{-D_{\text{Mn}}^{\text{Trans-int}}}{v\delta} \right) \right)$$

where  $X_{\text{Mn}}^I$  is the concentration of Mn within the interface,  $V_m$  is the molar volume,  $(\mu_{\text{Mn}}^\gamma - \mu_{\text{Mn}}^I)$  is the chemical potential difference of Mn between the austenite and the interface,  $\delta$  is the thickness of the interface (normally taken as 1 nm),  $v$  is the interface velocity, and  $M_{\text{Mn}}^{\text{Trans-int}}$  and  $D_{\text{Mn}}^{\text{Trans-int}}$  are the trans-interface mobility and diffusivity coefficients of Mn, respectively. The difference  $(\mu_{\text{Mn}}^\gamma - \mu_{\text{Mn}}^I)$  refers to Mn atom jumping from the interface into the austenite driven by the local chemical potential difference. The last term in the expression accounts for the “efficiency” of the Mn jump, which depends on the ratio of the residence time of the moving interface ( $\delta/v$ ) to the diffusion time across the interface ( $\delta^2/D_{\text{Mn}}$ ) [80]. This jump approach has been successfully used to explain similar phenomena as observed in this work that was experimentally found before in a Fe–C–Mn system under LENP conditions [32]. This behavior of Mn differs from that of Si, which jumps from the interface into  $\alpha_B$ , driven by the local chemical potential difference between the interface and  $\alpha_B$ . In this alloy the “efficiency” term and the chemical potential difference either between the interface and  $\gamma_R$  for Mn or between the interface and  $\alpha_B$  for Si are not sufficient to cause atomistic jumps from the interface into the  $\gamma_R$  or into  $\alpha_B$ , respectively. Furthermore, we suggest that the strong interaction between Mn and Si atoms at the  $\gamma_R/\alpha_B$  interface can lead to their increased accumulation.

Following this analysis, we suggest that the concentration spikes observed in the vicinity of the  $\gamma_R/\alpha_B$  interface for the 31SB-TRIP steels (Fig. 8) can locally lead to a solute drag effect during  $\alpha_B$  growth. In this context the Mn and Si spikes at the  $\gamma_R/\alpha_B$  interface can be quantified in terms of an accumulation factor  $\varepsilon = (\text{at.\% at the phase boundaries})/(\text{at.\% in the phases})$ . The values of  $\varepsilon$  for Mn and Si are  $1.82 \pm 0.05$  and  $1.48 \pm 0.15$ , respectively. These experiments show that the accumulation of Mn at the  $\gamma_R/\alpha_B$

interface has a stronger tendency to drag the  $\gamma$ -to- $\alpha_B$  transformation than that of Si. This difference in the accumulation factor at the  $\gamma_R/\alpha_B$  interface may be related to their different mobility values at elevated temperatures. This phenomenon represents an important kinetic effect in the bainitic transformation in SB-TRIP steels with high C content. Moreover, we propose that the prevailing equilibrium condition in the bainitic transformation in these steels can be designed by controlling the chemistry of the alloying elements (especially of the Si:Al ratio), considering an identical austempering temperature and time. It is important to note that the present alloys do not contain allotriomorphic ferrite and pearlite, which are generally formed in a reconstructive manner.

In addition to this local enrichment, very weak partitioning of Mn into the austenite phase and of Si into the ferrite phase was observed (Fig. 8). As the substitutional elements thus seem to play a role in the current bainitic transformation in the 31SB-TRIP steel, it should be discussed whether a PE or a local equilibrium mechanism prevailed. The observed Mn, C and Si concentration profiles

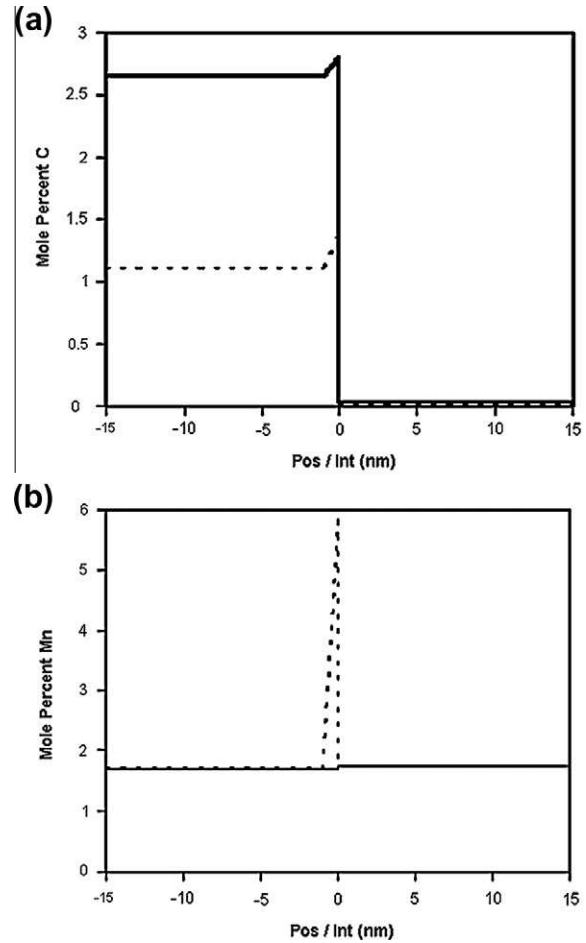


Fig. 13. Concentration profile of (a) C and (b) Mn across the interface under local equilibrium (LE) with negligible partitioning (LENP, dotted line) and under para-equilibrium (PE, dashed line) modes, obtained from the software DICTRA in an Fe–1.7 wt.% Mn–0.2 wt.% C alloy (taken from Ref. [39]).



indicate that the bainitic transformation in the 31SB-TRIP steel, austempered at 400 °C for 160 min, proceeds under LENP condition but not under either a PE or a local equilibrium with substitutional partitioning condition. The PE case is in the current work observed only for the 11SB-TRIP and 13SB-TRIP steels held at 400 °C. Typically, differences between LENP and PE, which reveal characteristic distributions of the substitutional elements involved (especially Si and Mn), are hard to determine by field ion microscopy [13] or APT [39] as the redistribution of the elements typically takes place over a few nanometers. However, DICTRA calculations have been carried out to elucidate which type of local equilibrium boundary condition is prevalent at the  $\alpha/\gamma$  interface in a low-carbon Fe–Mn–C alloy [39]. Fig. 13 displays the concentration profiles of C and Mn across the  $\gamma/\alpha$  interface under local equilibrium and PE conditions, calculated using the software DICTRA, for a Fe–1.72 wt.% Mn–0.18 wt.% C alloy (taken from Ref. [39]). These authors reported that a composition spread of the interface width at the interface could artificially be an effect of the spatial limits of the APT method due to a difference in the evaporation field between the  $\alpha$  and the  $\gamma$  phase. It was also reported that this composition spread at the grain boundaries in Ni-based superalloys can artificially extend up to a few nanometers, as determined by APT analysis [77]. Nevertheless, our APT result obtained from 31SB-TRIP steels austempered at 400 °C is in good agreement with DICTRA calculations (Fig. 13). Therefore, the current finding suggests that an APT experiment can distinguish and determine the equilibrium modes, either LENP or PE, prevailing at the  $\gamma_R/\alpha_B$  interface, in spite of possible differences in the evaporation fields. Thus, corresponding DICTRA calculations for the 31SB-TRIP alloy will be an interesting topic for future work, in order to validate the expected concentration values of the spikes.

In the 11SB-TRIP steel, we detected local accumulations of Si and Al atoms (both ferrite forming elements) in the vicinity of the cementite/ $\alpha_B$  interface (Fig. 9), in agreement with previous reports about a Si pile-up at the cementite/ferrite interface observed by field ion microscopy [81] and APT [26]. This observation can be attributed to the rejection of poorly soluble Si from cementite. The opposite result is found for Mn. Even though the APT observation of cementite precipitated at the  $\gamma_R/\alpha_B$  interface is a single data set, it provides direct evidence for the occurrence of cementite particles formed at the  $\gamma_R/\alpha_B$  interface in upper bainite. Typically, it is very hard to detect a nanometer-sized cementite precipitated at the  $\gamma_R/\alpha_B$  interface by other characterization means. Moreover, the present APT results support the theory proposed by Owen [82] on the suppressing effect of Si on cementite formation due to the sluggish rejection kinetics of Si atoms away from the moving heterointerface. Another important aspect is that Mn inside the cementite formed below 500 °C is more enriched than in the  $\gamma_R$  phase (Fig. 9c). This is a clear indication of the occurrence of Mn diffusion from  $\gamma_R$  into the cementite on

annealing at  $T \leq 500$  °C for 1 h. This observation indicates a deviation from the typical assumption that the mobility of Mn inside  $\gamma_R$  should be very limited, and, hence, Mn diffusion could be neglected. Dmitrieva et al. [24] reported that the calculated mean free path of Mn atoms in a face-centered cubic lattice using DICTRA simulations was only 2.5 nm at 450 °C for 48 h. We hence speculate that this Mn enrichment in the cementite rather than in  $\gamma_R$  in this alloy is not fully controlled by diffusion. More details have been published in Ref. [24].

Another point observed in this study is that the slight build-up of Al is also visible at the cementite/ $\alpha_B$  interface although Al exhibits a lower enrichment than Si (Fig. 9c). This means that the barrier for cementite nucleation is more effectively reduced by Si than by Al, which is in good agreement with our thermodynamic calculations (Fig. 12). This difference in the effects of Si and Al could be due to the higher mobility of Al in ferrite compared to that of Si during cementite growth at high temperatures as well as due to their different binding energies at the cementite/ $\alpha_B$  interface. Therefore, we conclude that Si and Al atoms can be segregated at the cementite/ $\alpha_B$  interface when the cementite forms and grows.

Based on the atomic-scale findings, we also suggest that the redistribution of substitutional elements at either  $\gamma_R/\alpha_B$  or cementite/ $\alpha_B$  interfaces can deteriorate the associated solid-solution strengthening effects since they are depleted in the grain interiors compared to the usually assumed nominal compositions.

## 5. Conclusions

We investigated the bainitic transformation in steels with 0.71 wt.% C from an atomistic perspective. Specific attention was placed on the roles of Si, Al and Mn as well as on the austempering temperature. The stability of  $\gamma_R$  in terms of its volume fraction, morphology and C content was studied at the subnanometer and micrometer scales. The mechanical properties of these alloys were also studied in order to lay out a pathway for an optimal and atomistically guided design of advanced SB-TRIP steels. The influence of the Si:Al ratio on the properties of the SB-TRIP steels can be summarized as follows. If the Si content is larger than the Al content, we observe an increased suppressing effect for cementite formation and growth. Conversely, if the Al content exceeds the Si content, we find accelerated bainitic transformation, higher partitioning of C into austenite and higher austenite stability. Besides these Si:Al effects, we make the following more general conclusions:

1. The mechanical properties of the steels vary significantly with the austempering temperature and with the Si:Al ratio. Upon decreasing the Si:Al ratio from 3:1 to 1:3, the YS, UE and toughness values increase, whereas the UTS decreases. Also, an increase in the IBT temperature from 400 to 430 °C leads to the reduction of YS, UE and toughness, while the UTS increases.

2. A decrease in the grain size of blocky-type  $\gamma_R$  is caused by lowering the Si:Al ratio and decreasing austempering temperature, while the bainitic transformation is accelerated by these two parameters. For the steels studied in this work, the volume fraction of  $\gamma_R$  is not greatly affected by the Si:Al ratio or the austempering temperature, rather the size and dispersion of the blocky-type  $\gamma_R$  may change. In addition, an important observation is that the influence of the austempering temperature on the mechanical properties is suppressed with decreasing the Si:Al ratio.
3. We detected an increase in the C concentration in  $\gamma_R$  upon lowering the Si:Al ratio and the austempering temperature, which leads to an enhanced thermal stability of  $\gamma_R$ . Considering the observed microstructural evolution of  $\gamma_R$ , we found that the highest thermal stability of  $\gamma_R$  for a low Si:Al ratio (13SB-TRIP steels) and a low austempering temperature (400 °C), which is related to the increased C content in  $\gamma_R$ . The transformation of  $\gamma_R$  into deformation-induced martensite during tensile loading can be effectively suppressed in these 13SB-TRIP steels.
4. Using APT, we studied elemental redistribution phenomena across the phase boundaries in the SB-TRIP steels as well as cementite precipitation formed at the  $\gamma_R/\alpha_B$  interface. We found experimental evidence for the solute drag effect of Si and Mn atoms in the vicinity of the  $\gamma_R/\alpha_B$  interface, suggesting that the mechanism of bainitic phase transformation in the 31SB-TRIP steels austempered at 400 °C can occur under local equilibrium with some minor partitioning (of Mn and Si), i.e. essentially in the negligible partitioning mode. We propose that there is a local competition between local equilibrium with negligible partitioning and PE modes depending on the alloy composition, specifically on the Si:Al ratio.

Overall, the newly designed and thermally processed SB-TRIP steels presented in this work show an excellent combination of strength and elongation at very good impact toughness values, rendering them suitable for advanced automotive applications.

## Acknowledgements

The authors are grateful to POSCO R&D and BK21 for supplying the alloy samples and for financial support. We are acknowledging the help of Mr. J.W. Jung, Prof. Y.W. Jang (POSTECH) and Dr. S.G. Hong (POSCO) for fruitful discussions. The authors also thank Dr. B.H. Lee (NCNT) for APT analysis.

## References

- [1] Chung JH, Jeon JB, Chang YW. *Met Mater Int* 2010;16:533–41.
- [2] Abareshi M, Emadoddin E. *Mater Design* 2011;32:5099–105.
- [3] Zaefferer S, Ohlert J, Bleck W. *Acta Mater* 2002;52:2765–78.
- [4] De Cock T, Ferrer JP, Capdevila C, Caballero FG, López V, García de Andrés C. *Scripta Mater* 2006;55:441–3.
- [5] Van Slycken J, Verleysen P, Dergriek J, Bouquerel J, De Cooman BC. *Mater Sci Eng A* 2007;460–461:516–24.
- [6] De Cooman BC. *Curr Opin Solid State Mater Sci* 2004;8:285–303.
- [7] Matlock DK, Speer JG. *Proc 3rd Int Conf on advanced structural steels, KIM. Gyeongjoo, Korea; 2006. p. 744–81.*
- [8] Van der Zwaag S, Zhao L, Kruijver SO, Sietsma J. *ISIJ Int* 2002;42:1565–70.
- [9] Suh DW, Park SJ, Oh CS, Kim SJ. *Scripta Mater* 2007;57:1097–100.
- [10] Mahieu J, Maki J, De Cooman BC, Fiorucci M, Claessens S. *Mater Sci Technol* 2003;19:125–31.
- [11] Suh DW, Park SJ, Oh CS, Kim SJ. *Metal Mater Trans* 2010;41A:397–408.
- [12] Bellhouse E, Mertens A, McDermid J. *Mater Sci Eng A* 2007;463:147–56.
- [13] Bhadeshia HKDH, Edmonds DV. *Acta Metall* 1980;28:1265–73.
- [14] Pichler A, Stiaszny P, Potxinger R, Tikal R, Werner E. *Proc 40th Int Conf on mechanical working and steel processing. Iron and Steel Society; 1998. p. 259–74.*
- [15] Garcia-Mateo C, Caballero FG, Bhadeshia HKDH. *ISIJ Int* 2003;43:1821–5.
- [16] Caballero FG, Bhadeshia HKDH, Mawella KJA, Jones DG, Brown P. *Mater Sci Technol* 2001;17:517–22.
- [17] Caballero FG, Miller MK, Babu SS, Garcia-Mateo C. *Acta Mater* 2007;55:381–90.
- [18] Caballero FG, Santofimia MJ, Garcia-Mateo C, Chao J, García de Andrés C. *Mater Design* 2009;30:2077–83.
- [19] Caballero FG, Miller MK, Babu SS, Garcia-Mateo C, Capdevila C, Babu SS. *Acta Mater* 2008;56:188–99.
- [20] Choi P, da Silva M, Klement U, Al-Kassab T, Kirchheim R. *Acta Mater* 2005;53:4473–81.
- [21] Miller MK, Forbes RG. *Mater Charact* 2009;60:461–9.
- [22] Seol JB, Gu GH, Lim NS, Das S, Park CG. *Ultramicroscopy* 2010;110:783–8.
- [23] Seol JB, Lim NS, Lee BH, Renaud L, Park CG. *Met Mater Int* 2011;17:413–6.
- [24] Dmitrieva O, Ponge D, Inden G, Millan J, Choi P, Sietsma J, et al. *Acta Mater* 2011;59:364–74.
- [25] Pereloma EV, Timokhina IB, Miller MK, Hodgson PD. *Acta Mater* 2007;55:2587–98.
- [26] Pereloma EV, Beladi H, Zhang L, Timokhina IB. *Metal Mater Trans* 2011, in press. <http://dx.doi.org/10.1007/s11661-011-0782-0>.
- [27] Bhadeshia HKDH, Waugh AR. *Acta Mater* 1982;30:775–84.
- [28] Hillert M. *Paraequilibrium*. Stockholm: Institute for Metals Research; 1953.
- [29] Hultgren A. *Trans ASM* 1947;39:915.
- [30] Aaronson HI, Domain HA. *Trans AIME* 1966;236:781.
- [31] Zurob HS, Hutchinson CR, Beche A, Bréchet Y, Seyedrezai H, Purdy GR. *Acta Mater* 2008;56:2203.
- [32] Zurob HS, Hutchinson CR, Bréchet Y, Seyedrezai H, Purdy GR. *Acta Mater* 2009;57:2781–92.
- [33] Kozesnick E. *Calphad* 2000;24(4):495.
- [34] Vitek J, Babu SS, Kozesnick E. In: Damm, Merwin, editors. *Austenite formation and decomposition*. Warrendale, PA: TMS; 2003. p. 139.
- [35] Saha A, Ghosh G, Olson GB. *Acta Mater* 2005;53:141.
- [36] Guo H, Purdy GR, Enomoto M, Aaronson HI. *Metall Mater Trans* 2006;37A:1721–9.
- [37] Guo H, Enomoto M. *Metall Mater Trans* 2007;38A:1152–61.
- [38] Capdevila C, Cornide J, Tanaka K, Nakanishi K, Urones-garrote E. *Metall Mater Trans* 2011;42A:3719–28.
- [39] Thuillier O, Danoix F, Gouné M, Blavette D. *Scripta Mater* 2006;55:1071–4.
- [40] Flectcher HA, Garratt-Reed AJ, Aaronson HI, Purdy Jr GR, Reynolds WT, Smith GDW. *Scripta Mater* 2001;45:561.
- [41] Ghosh G, Olson GB. *Acta Mater* 2002;50:2099.

- [42] Mahieu J, Maki J, De Cooman BC, Claessens S. *Metall Mater Trans* 2002;33A:2573.
- [43] Herrera C, Ponge D, Raabe D. *Acta Mater* 2011;59:4653.
- [44] Springer H, Kostka A, Payton EJ, Raabe D, Kaysser-Pyzalla A, Eggeler G. *Acta Mater* 2011;59:1586.
- [45] Jateczak CF. SAE technical paper series 800426, SAE, PA; 1980. p. 1–20.
- [46] Sundman B, Jansson B, Andersson JO. *Calphad* 1985;9:153–90.
- [47] Chin KG, Lee HJ, Kwak JH, Kang JY, Lee BJ. *J Alloys Compd* 2010;505:217–23.
- [48] Takahashi M. Nippon steel. Tech. rep. no. 88; 2003.
- [49] Larson DJ, Foord DT, Petford-Long AK, Liew H, Blamire MG, Cerezo A, et al. *Ultramicroscopy* 1999;79:287–93.
- [50] Miller MK, Russell KF, Thompson GB. *Ultramicroscopy* 2005;102:287–98.
- [51] Tirumalasetty GK, van Huis MA, Kwakernaak CK, Sietsma J, Sloof WG, Zandbergen HW. *Acta Mater* 2012;60:1311.
- [52] Dmitrieva O, Choi P, Gestl SSA, Ponge D, Raabe D. *Ultramicroscopy* 2011;111:623.
- [53] Li YJ, Choi P, Borchers C, Chen YZ, Goto S, Raabe D, et al. *Acta Mater* 2011;59:3965–77.
- [54] Voronin VI, Berger IF, Gornostyrev YN, Urtsev VN, Kuznetsov AR, Shmarkov AV. *JETP Lett* 2010;91:143–6.
- [55] Vella A, Vurpillot F, Gault B, Bostel A, Menand A, Deconihout B. *Phys Rev B* 2006;73:165416.
- [56] Vurpillot F, Gault B, Vella A, Bouet M, Deconihout B. *Appl Phys Lett* 2006;88:094105.
- [57] Cerezo A, Smith GDW, Clifton PH. *Appl Phys Lett* 2006;88:154103.
- [58] Sha G, Springer SP. *Ultramicroscopy* 2009;109:580.
- [59] Vermeulen AC, Delhez R, De Keijser ThH, Mittermeijer EJ. *J Appl Phys* 1995;77:5026–49.
- [60] Caballero FG, Garcia-Mateo C, Santofimia MJ, Miller MK, García de Andrés C. *Acta Mater* 2009;57:8.
- [61] Samek L, De Moor E, Penning J, De Cooman BC. *Metall Mater Trans A* 2006;37A:109–24.
- [62] Saha A, Jung J, Olson GB. *J Computer-Aided Mater Des* 2007;14:201–33.
- [63] Timokhina IB, Hodgson PD, Pereloma EV. *Metall Mater Trans* 2003;34A:1599–609.
- [64] Jimenez-Melero E, van Dijk NH, Zhao L, Sietsma J, Offerman SE, Wright JP. *Scripta Mater* 2007;56:421.
- [65] van Dijk NH, Butt AM, Zhao L, Sietsma J, Offerman SE, Wright JP. *Acta Mater* 2005;53:5439–47.
- [66] Ludwigson DC, Berger JA. *ISIJ Inst* 1969;207:63–9.
- [67] Olson GB, Cohen M. *Metall Trans* 1975;6A:791–5.
- [68] Tomota Y, Tokuda H, Adachi Y, Wakita M, Moriai A, Moriai A. *Acta Mater* 2004;52:5737–45.
- [69] Jacques PJ, Furnémont Q, Lani F, Pardoën T, Delannay F. *Acta Mater* 2007;55:3681–93.
- [70] Tirumalasetty GK, van Huis MA, Kwakernaak C, Sietsma J, Sloof WG, Zandbergen HW. *Acta Mater* 2012;60:1311–21.
- [71] de Moor E, Lacroix S, Clarke AJ, Penning J, Speer JG. *Metal Mater Trans* 2008;39A:2586–95.
- [72] Park KK, Oh ST, Baeck SM, Kim DI, Han JH, Han HN. *Mater Sci Forum* 2002;408–412:571–6.
- [73] Sietsma J, van der Zwaag S. *Acta Mater* 2004;52:4143–52.
- [74] Hutchinson CR, Fuchsmann A, Brechet Y. *Metall Mater Trans* 2004;35A:1211.
- [75] Bos C, Sietsma J. *Scripta Mater* 2007;57:1085.
- [76] Blavette D, Vurpillot F, Pareige P, Menand A. *Ultramicroscopy* 2001;89:145.
- [77] Blavette D, Duval P, Letellier L, Guttman M. *Acta Mater* 1996;44(12):4995.
- [78] Militzer N, Mecozzi MG, Sietsma J, van der Zwaag S. *Acta Mater* 2006;54:3961–72.
- [79] Lücke K, Stüwe HP. *Acta Metall* 1971;19:1087.
- [80] Kirkaldy JS, Thomson BA, Baganis EA. In: Doane EV, Kirkaldy JS, editors. *Hardenability concepts with applications to steel*. Warrendale, PA: TMS-AIME; 1978. p. 82–125.
- [81] Chang L, Smith GDW. *J Phys* 1984;C9(1):397.
- [82] Owen WS. *Trans ASM* 1954;46:812–29.